Journal of Materials Chemistry A

ROYAL SOCIETY OF CHEMISTRY

PAPER

View Article Online
View Journal | View Issue

Cite this: J. Mater. Chem. A, 2025, 13, 35400

Hybrid polysaccharide–NaI derived transparent and flexible solid-state electrolyte films for sustainable design of supercapacitors

Sushant Wakekar,[a] Bapan Jana,[b] Saisrinu Yarramsetti,[a] Samrat Ghosh,[c] Laxmi Narayana Patro,[d] Pardha Saradhi Maram,[a] Maheswaran Shanmugam[b] and Chinmoy Das *[a]

Conventional liquid electrolytes utilized in supercapacitors suffer from leakage, flammability, and poor adaptability making them unsuitable to design flexible, wearable, and portable devices. Despite the significant advancements in designing flexible electrode materials towards the fabrication of safer and integrated energy storage systems, the development of optically transparent and mechanically flexible polysaccharide-based solid-state electrolytes remains comparatively limited. Herein, we report a series of flexible solid-state electrolyte ($FSSE_{NaI-x}$; where x = 27, 43, 53, 60, 65, and 69 wt%) films, composed of konjac glucomannan (KGM), hydroxypropyl methylcellulose (HPMC), and sodium iodide (NaI). Among them, the $FSSE_{NaI-65}$ film exhibits optimal properties in terms of mechanical, optical, and ionic conductivity suitable for designing supercapacitor devices. It achieves a Young's modulus of ~2.5 MPa with an exceptional elongation at break at 118%, along with an optical transparency of 88% at 800 nm. It delivers a high ionic conductivity of 2.77 mS cm^{-1} at room temperature and a wide electrochemical stability window of 2.4 V. A solid-state supercapacitor assembled with the $FSSE_{NaI-65}$ film shows a specific capacitance of 159 F g^{-1} at 1 A g^{-1}, with an excellent cycling stability retaining 87.5% of its specific capacitance over 4000 cycles at 5 A g^{-1}. It maintains a stable performance under bending conditions with a capacitance retention of 72.2% over 2000 cycles at 5 A g^{-1}. The device furnishes a high energy density of 22.1 Wh kg^{-1} and power density of 500.6 W kg^{-1} at 1 A g^{-1} confirming its potential for next-generation flexible energy storage systems.

Received 30th May 2025
Accepted 6th September 2025

DOI: 10.1039/d5ta04374c

rsc.li/materials-a

[a]Department of Chemistry, SRM University-AP, Amaravati, Andhra Pradesh-522240, India. E-mail: chinmoy.d@srmap.edu.in
[b]Department of Chemistry, Indian Institute of Technology Bombay, Powai, Mumbai, Maharashtra-400076, India
[c]Inorganic and Physical Chemistry Laboratory, Council of Scientific and Industrial Research (CSIR), Central Leather Research Institute (CLRI), Chennai-600020, India
[d]Department of Physics, SRM University-AP, Amaravati, Andhra Pradesh-522240, India

Chinmoy Das

Chinmoy Das received his PhD in Inorganic Chemistry from the Indian Institute of Technology Bombay in 2018. He pursued postdoctoral research at the AIST–Kyoto University Chemical Energy Materials Open Innovation Laboratory (CHEM-OIL), Japan (2018–2021), followed by another postdoctoral stint at Technische Universität Dortmund (TU Dortmund), Germany (2021–2023). In 2023, he returned to India to join SRM University-AP, Andhra Pradesh, as an Assistant Professor. His research interests focus on the design and synthesis of coordination network-based materials for applications in solid-state batteries and supercapacitors, atmospheric water harvesting, and photoluminescent glasses.

Introduction

Electrochemical energy storage devices have become an integral part of modern society and are capable of storing renewable energy. Among these, supercapacitors and rechargeable batteries stand out as efficient, eco-friendly, and cost-effective power solutions.[1] They play a significant role in powering electric and hybrid vehicles, where improving energy density and expanding the operating voltage range are crucial for extending the driving range. Electric double-layer capacitors (EDLCs) have become a vital energy storage technology due to their high-power density, fast charge–discharge capability, and long cycle life.[2,3] Unlike conventional batteries that store energy through faradaic redox reactions, EDLCs operate based on electrostatic charge accumulation at the electrode–electrolyte interface, forming an electric double layer. This mechanism enables ultrafast energy storage and release, making EDLCs highly efficient for applications requiring rapid power delivery.[4,5] Building upon the advantages of traditional EDLCs, flexible EDLCs have emerged as a breakthrough in energy storage, offering mechanical adaptability alongside high electrochemical performance. Designed with bendable, transparent, and stretchable materials for electrodes and electrolytes, these capacitors maintain stability even under significant deformation. This unique combination makes flexible EDLCs ideal for next-generation wearable electronics, soft robotics, and foldable displays. These energy storage devices must be thin, light weight, and mechanically adaptable while also being cost-effective and biodegradable to ensure long-term sustainability.[6–9]

To address these needs, all-solid-state flexible supercapacitors based on polymer electrolytes have emerged as a promising solution. Polymer electrolytes offer mechanical flexibility, high ionic conductivity, and a wide electrochemical window, enabling efficient energy storage in devices that can bend, stretch, and conform to various shapes.[6] Polymers, such as poly(ethylene oxide) (PEO),[10] poly(vinylidene fluoride) (PVDF),[11] poly(acrylonitrile) (PAN),[12] and poly(methyl methacrylate) (PMMA),[13] along with the incorporation of conducting salts, ionic liquids, or both, have been reported for developing electrolytes. Although these electrolytes have been demonstrated to be effective materials for fabricating energy storage devices, they raise significant concerns due to their non-biodegradability in the environment.[14–16] Moreover, the shift toward biodegradable polymer electrolytes and non-pyrolyzed electrolyte materials is crucial in reducing environmental impact while maintaining high energy storage efficiency.[17] By integrating biodegradable and cost-effective materials, flexible supercapacitors can revolutionize wearable electronics and portable energy storage, fostering sustainable, high-performance energy solutions that will drive the next generation of eco-friendly smart devices and flexible electronic technologies.[18]

The rapid growth of portable and transparent electronics has further intensified the need for advanced energy storage systems.[19] While transparent electronics such as displays, transistors, and memory devices have progressed significantly, energy storage devices with high optical transparency and mechanical flexibility are yet to be realized.[20] Transparent supercapacitors have emerged as promising candidates, offering efficient energy storage, fast response, long lifespan, and cost-effective fabrication. With the rise of smart technologies such as transparent displays, wearable health monitors, smart windows, and solar-powered systems, the demand for transparent, flexible, and lightweight power sources is more pressing than ever.[19,21] Mechanically flexible and optically transparent supercapacitors are especially well-suited for this role, delivering reliable performance even under bending or stretching and aligning well with the needs of next-generation flexible electronics.[6,9] They are also being considered for integration into advanced bioelectronic platforms such as smart contact lenses, electronic skins, and real-time health monitoring systems. Their transparency allows for visual integration and biological signal monitoring, while their flexibility ensures seamless conformance to soft or curved surfaces for biomedical and wearable applications.[22,23]

Here, in this study, we report flexible solid-state electrolyte ($FSSE_{NaI\text{-}x}$; where $x = 27$, 43, 53, 60, 65, and 69 wt%) films, obtained from *in situ* gelation of konjac glucomannan (KGM), hydroxypropyl methylcellulose (HPMC), and sodium iodide (NaI) in water. Among the various weight percentage $FSSE_{NaI}$ films made, the $FSSE_{NaI\text{-}65}$ film imparts exceptional mechanical flexibility, transparency, robust structural integrity, and enhanced ionic conductivity to the material. The $FSSE_{NaI\text{-}65}$ film exhibits a high ionic conductivity of 2.77 mS cm^{-1} and delivers a specific capacitance of 159 F g^{-1} at a current density of 1 A g^{-1}. Moreover, it demonstrates outstanding electrochemical durability, retaining 87.5% of its initial capacitance after 4000 charge–discharge cycles. Even upon structural deformation, the $FSSE_{NaI\text{-}65}$ film retains excellent electrochemical characteristics with a capacitance retention of 72.2% after 2000 cycles. The incorporation of natural polysaccharide components not only enhances sustainability but also contributes to the electrolyte's favourable mechanical and electrochemical behaviour. Furthermore, symmetric supercapacitor devices assembled using the FSSE film achieve an energy density of 22.11 Wh kg^{-1} and a power density of 500.6 W kg^{-1} at 1 A g^{-1}. These results highlight the potential of this sustainable solid-state electrolyte in flexible and wearable energy storage systems, particularly emphasising the synergy between high performance and mechanical resilience.

Results and discussion

Syntheses, composition, and structural analysis

Flexible solid-state electrolyte ($FSSE_{NaI\text{-}x}$; where $x = 27$, 43, 53, 60, 65, and 69 wt%) films are synthesized through a rapid and economically viable pour casting method (Fig. 1, S1 and Table S1; see the Method section in the SI). In a representative synthesis, NaI was first dissolved in distilled water to form a clear solution. Subsequently, KGM and HPMC were gradually added to the NaI solution under continuous stirring, leading to the formation of a gel-like material which was poured onto a Petri dish and allowed to settle and evenly disperse. Upon

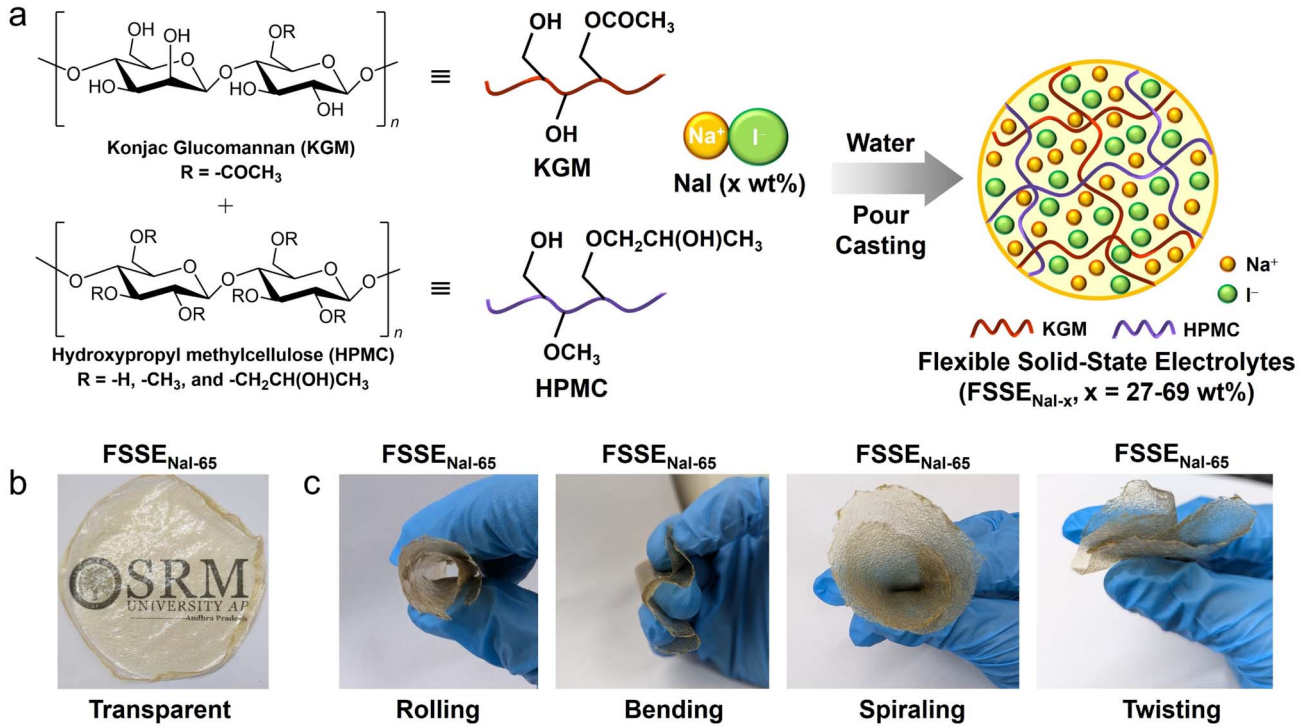

Fig. 1 (a) Schematic representation for the preparation of flexible solid-state electrolytes ($FSSE_{NaI\text{-}x}$, x = 27–69 wt%). (b) An image of a representative transparent film of $FSSE_{NaI\text{-}65}$. (c) Photographs of various modes of flexibility of a representative $FSSE_{NaI\text{-}65}$ film.

drying for 24–48 hours under ambient conditions, a transparent film was obtained. This gelation method was attained *via* self-agglomeration through H-bonding without adding any chemical crosslinkers or initiators.[24]

Scanning electron microscope (SEM) images revealed the smooth surface of the synthesized films ($FSSE_{NaI\text{-}x}$; where x = 27, 43, 53, 60, 65, and 69 wt%) indicating characteristic features of amorphous behaviour (Fig. 2a–f). The energy dispersive X-ray analysis (EDAX) has been performed on a specific area of the synthesized films ($FSSE_{NaI\text{-}x}$; where x = 27, 43, 53, 60, 65, and 69 wt%). The increase in the Na^+-ion concentration (in weight% or atomic%) well aligns with the gradual increment of NaI content during the preparation (Fig. S2).

In addition, CHN analysis suggested a gradual decrease in % C and % H elements across the films which agreed with the synthesis method discussed in the SI (details of methods, Table S2).

We characterized $FSSE_{NaI\text{-}x}$ (where x = 27, 43, 53, 60, 65, and 69 wt%) films through powder X-ray diffraction (PXRD) studies to understand their crystalline and/or amorphous features. The X-ray diffraction pattern of NaI exhibits strong, sharp peaks, due to its highly crystalline nature. On the other hand, KGM shows a broad, diffusely scattered peak characteristic of its amorphous nature.[24] In contrast, HPMC exhibits two broad characteristic diffraction peaks at $2\theta = 8°$ and 21°, indicating its semicrystalline behaviour.[25] Interestingly, all the synthesized FSSE films showed diffused scattering in the PXRD pattern (Fig. 2g). The flattening and broadening of the diffraction pattern in the films suggest good miscibility between KGM, HPMC, and NaI. The effective miscibility of the components in the gel phase results in enhanced mechanical stability, suppresses phase separation, and facilitates ion mobility.[26,27]

The structural features of $FSSE_{NaI\text{-}x}$ (x = 27, 43, 53, 60, 65, and 69 wt%) films were elucidated through Fourier transform infrared spectroscopy (FT-IR) (Fig. 2h). The vibration bands of KGM were observed at approximately 3295 cm^{-1} and 2883 cm^{-1}, corresponding to the stretching vibrations of –OH groups and the C–H bonds of methyl groups, respectively. Additionally, in KGM, characteristic vibration bands of mannose (β-1,4-C–O–C linkage) appeared at 870 cm^{-1} and 798 cm^{-1}.[24] On the other hand, in HPMC, the stretching vibration band at around 3420 cm^{-1} was attributed to O–H asymmetric stretching, while the band near 2904 cm^{-1} corresponded to C–H asymmetric stretching. The vibration band at 1049 cm^{-1} was assigned to C–O–C stretching vibration of polysaccharide rings. Furthermore, the vibrations at 1455 cm^{-1} and 1315 cm^{-1} were associated with the asymmetric and symmetric bending vibrations of the methyl group in $–CH_3O$. In addition, the H–O–H bending vibration was detected as a stronger band at 1639 cm^{-1}. A shift in –OH stretching vibration due to 3394 cm^{-1} suggests the formation of hydrogen bonding between the –OH groups of HPMC (3420 cm^{-1}) and KGM (3295 cm^{-1}).[24] Incorporation of NaI into the polysaccharide network matrices causes the enhancement of band intensity at 1640 cm^{-1} which suggests that the Na^+ ions are interacting with the C–O or –OH groups of polysaccharides, forming a bond between them and resulting in a more stable and homogeneous composite material.[28] The intrinsic vibrational bands of KGM and HPMC observed in the films indicate that each polysaccharide retains its individual characteristic

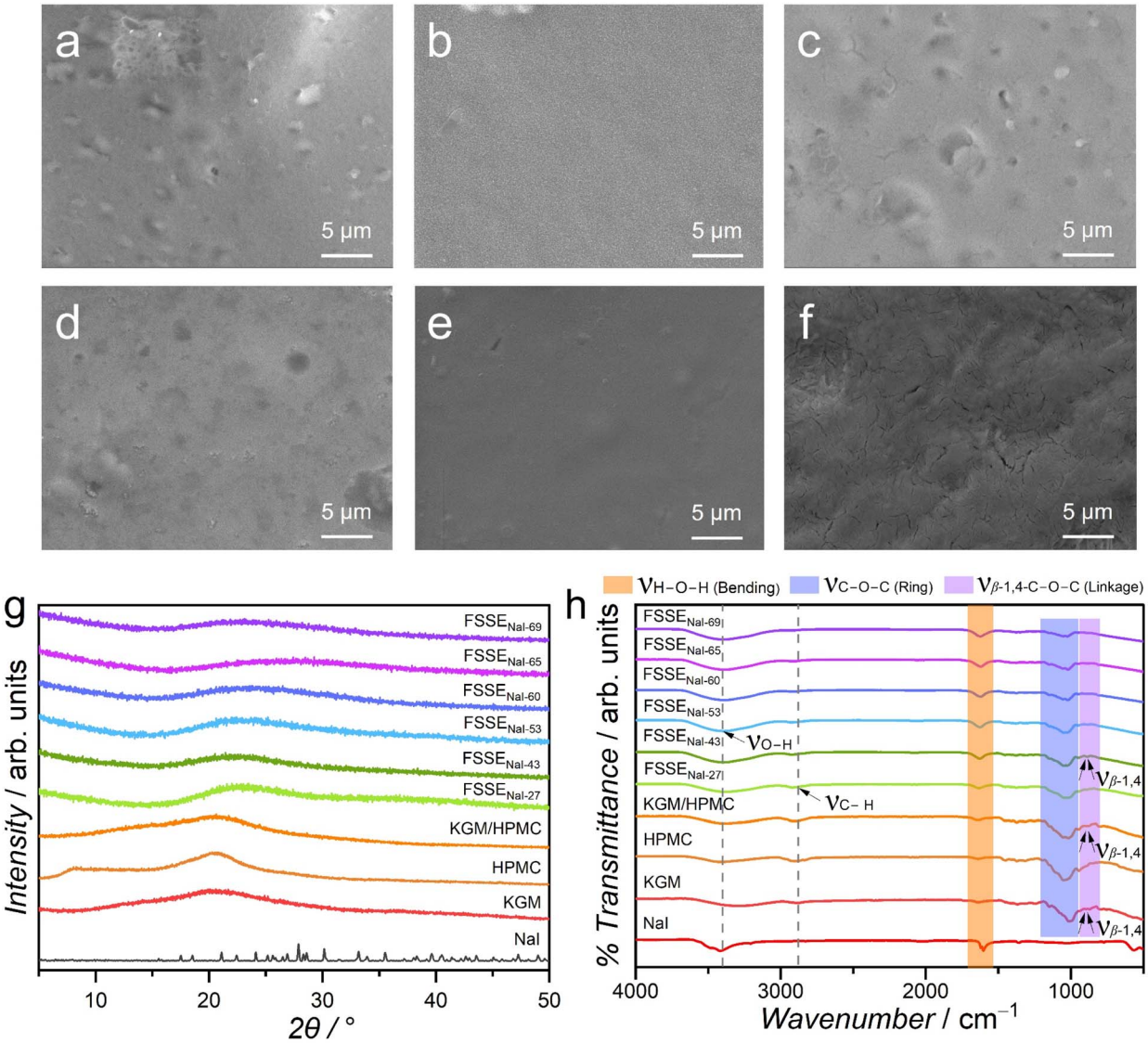

Fig. 2 (a–f) Scanning electron microscope (SEM) images of FSSE$_{NaI-x}$ (x = 27, 43, 53, 60, 65, and 69 wt%) films. Scale bar: 5 μm. (g) Powder X-ray diffraction (PXRD) patterns of NaI, KGM, HPMC, KGM/HPMC film, and FSSE$_{NaI-x}$ (x = 27, 43, 53, 60, 65, and 69 wt%) films. (h) Fourier transform infrared (FT-IR) spectra of NaI, KGM, HPMC, KGM/HPMC blend film, and FSSE$_{NaI-x}$ (x = 27, 43, 53, 60, 65, and 69 wt%) films.

behavior. To corroborate the FT-IR results, Raman spectra of pure NaI and as-synthesized FSSE$_{NaI-x}$ (where x = 27, 43, 53, 60, 65, and 69 wt%) films were recorded in the range of 1610–1640 cm^{-1} (Fig. S3). Weak (~1616 cm^{-1}) and moderate (~1629 cm^{-1}) vibration bands correspond to the H–O–H bending vibration of water bound to hygroscopic NaI. With increasing NaI content, these bands shifted to higher frequencies, indicating progressive replacement of polysaccharide–water hydrogen bonds by a stronger Na^+–water hydration shell. This enhanced hydration shell facilitates faster Na^+ migration, improving ionic conductivity and electrochemical performance in FSSE$_{NaI-65}$ and FSSE$_{NaI-69}$.[29–32]

Thermal analysis of dehydrated films

The standalone FSSE$_{NaI-x}$ (x = 27, 43, 53, 60, 65, and 69 wt%) films are substantially stable through the hydrogen bonding network structure provided by water as a solvent.[28] To understand the thermal stability of FSSE films, we performed thermogravimetric analysis/differential thermal analysis (TGA/DTA) on the as-synthesized FSSE$_{NaI-x}$ (x = 27, 43, 53, 60, 65, and 69 wt%) films. A gradual weight loss was observed in each FSSE film due to removal of water molecules from the polysaccharide matrix. Beyond 220 °C, the films were inclined to thermal decomposition (Fig. S4). They were further activated at 105 °C for 10 hours to achieve a dehydrated state to comprehend the thermal stability of the films in the absence of water. TGA revealed that the network structure of films was thermally stable up to 200–230 °C with <1% weight loss at the onset temperature (Fig. S5). The thermal stability of dehydrated films deteriorated gradually with the incremental concentration of NaI (from 27 wt% to 69 wt%) and subsequent reduction of polysaccharide content in the network structure. Beyond the stable

temperature regime, there is a weight loss attributed to the breaking of glycosidic bonds within the polysaccharide matrix. This leads to the formation of monomeric units which facilitate the thermal degradation of the films. The decomposition of films was observed above 600 °C *via* the process of pyrolysis.[33]

We have performed differential scanning calorimetry (DSC) of dehydrated $FSSE_{NaI\text{-}x}$ ($x = 27$, 43, 53, 60, 65, and 69 wt%) films to understand the structural relaxation and chain dynamics during heating–cooling cycles (Fig. S6 and S7). During the first heating scan, the appearance of a single glass transition temperature (T_g) at around 110 °C for $FSSE_{NaI\text{-}x}$ ($x = 27$, 43, 53, and 60 wt% or ≤60 wt%) films was observed (Fig. S6). This endothermic phenomenon occurs due to the relaxation of internal stresses as the film transitions toward a more thermodynamically stable structure. During the second heating scan, we observed a broad T_g for FSSE films suggested that the materials have already undergone sufficient molecular reorganization, reduced free volume and eliminated residual stresses (Fig. S7). In contrast, during the first heating scan of $FSSE_{NaI\text{-}x}$ (x > 60 wt%) films, interestingly, two distinct T_g events emerged (Fig. S6). For the $FSSE_{NaI\text{-}65}$ film, we observed two apparent T_g at 60 °C and 76 °C, whereas for the $FSSE_{NaI\text{-}69}$ film, T_g appeared at 53 °C and 75 °C. This is indicative of microphase separation within the matrix into NaI-rich and NaI-deficient polymer domains with differing polymer chain dynamics.[34,35] In addition, for $FSSE_{NaI\text{-}x}$ (x > 60 wt%) films, we observed that a series of exothermic events appeared in the region of 150–200 °C during the heating scan, likely due to the thermal crystallization of NaI-rich domains (Fig. S6). This observation is corroborated through NaI crystalline phases that appeared in PXRD measurements on thermally dehydrated/activated films (Fig. S8). No observable transitions are detected during the cooling cycles of both the first and second DSC scans for $FSSE_{NaI\text{-}x}$ (x > 60 wt%) films, indicating thermal stability and a predominantly amorphous structure.

Mechanical and optical characteristics of $FSSE_{NaI\text{-}27}$ and $FSSE_{NaI\text{-}65}$ films

To understand the flexible behaviour of the films, we performed the mechanical studies on $FSSE_{NaI\text{-}x}$ ($x = 27$, 43, 53, 60, 65, and 69 wt%) films.

The mechanical properties of FSSE films reveal a clear transition from a rigid and brittle phase to a highly flexible and ductile phase upon increasing NaI content (Fig. 3a, b and S9; Table S3). This feature likely arises from the disruption of the hydrogen-bonding network, which becomes progressively loosened with increasing NaI content. $FSSE_{NaI\text{-}27}$ demonstrates a high tensile strength of ~22 MPa with a Young's modulus reaching 1188 MPa, indicative of the stiff behaviour of the film (Fig. 3b). This film undergoes fracture at a low strain of ~6%,

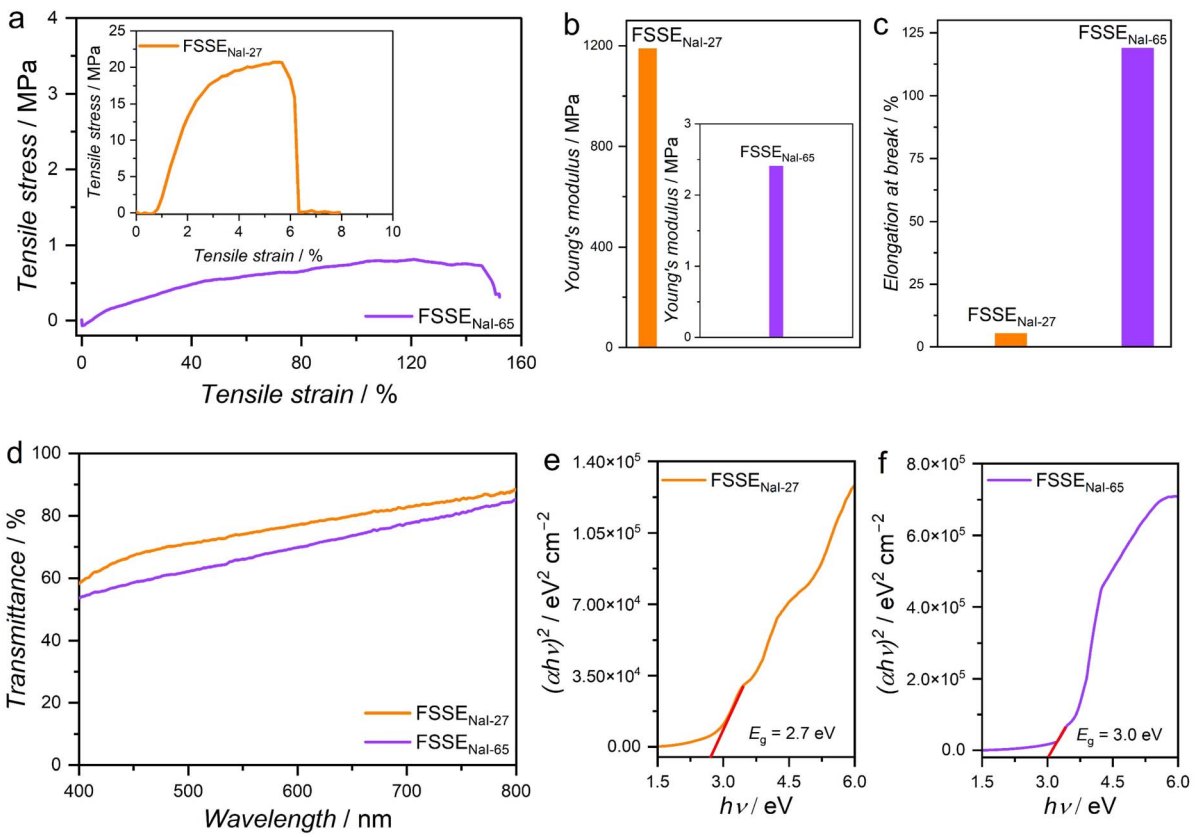

Fig. 3 (a) Curves of tensile stress (MPa) under tensile strain (%) for $FSSE_{NaI\text{-}65}$ and $FSSE_{NaI\text{-}27}$ (inset) films. (b) Comparison of Young's modulus (MPa) of $FSSE_{NaI\text{-}27}$ and $FSSE_{NaI\text{-}65}$ (inset) films. (c) Comparison plot of elongation at break (%) for $FSSE_{NaI\text{-}27}$ and $FSSE_{NaI\text{-}65}$ films. (d) Comparison of solid-state UV-Vis spectra of $FSSE_{NaI\text{-}27}$ and $FSSE_{NaI\text{-}65}$ films. (e and f) Tauc plots of $FSSE_{NaI\text{-}27}$ and $FSSE_{NaI\text{-}65}$ films.

reflecting its poor deformability and brittleness. In contrast, $FSSE_{NaI-65}$ exhibits significantly different mechanical features, with a substantial reduction in tensile strength to ~0.9 MPa and Young's modulus of ~2.4 MPa, but an exceptional elongation at break at 118% (Fig. 3c). This substantial increase in strain tolerance features the enhanced flexibility and ductility of the NaI-rich composition in the $FSSE_{NaI-65}$ film. However, further increasing the NaI concentration to 69 wt% (in the $FSSE_{NaI-69}$ film) results in a drastic decrease in elongation at break at ~43.50% maintaining its similar tensile strength; nevertheless there is a negligible increment in the Young's modulus value of ~3.7 MPa compared to the $FSSE_{NaI-65}$ film (Fig. S9 and Table S3). This flexibility decline in $FSSE_{NaI-69}$ is likely due to the excessive ionic interference with hydrogen bonds leading to a breakdown of the polymer network associated with reduced cohesive strength and loss of structural integrity. In contrast, many conventional synthetic polymer electrolytes exhibit lower mechanical properties, such as PEO@PI and PEO/CMC–Li@PI having a tensile strength of 4.29 and 6.47 MPa, respectively,[36] and tensile strength of PEO/SA–SPE is up to 3.57 MPa,[33] and PEO/PVDF/$LiClO_4$/SN based polymeric electrolyte achieved a maximum stress of 3.37 MPa.[37] The soft mechanical character of $FSSE_{NaI-65}$, together with its ability to undergo large deformations without fracture, suggests its suitability for flexible supercapacitor device fabrication.[26,38]

The optical characteristics of the $FSSE_{NaI-x}$ ($x = 27$, 43, 53, 60, 65, and 69 wt%) films with different NaI contents were evaluated through UV-Vis spectroscopy (Fig. 3d and S10) to understand the extent of transparency in the synthesized films. The transmittance (%) spectra reveal that $FSSE_{NaI-27}$ exhibits higher optical transparency across the visible region (400–800 nm) compared to $FSSE_{NaI-65}$ (Fig. 3d). Apparently, the $FSSE_{NaI-27}$ film achieves 88% transmittance at a longer wavelength (800 nm) moving from 58% transmittance in a shorter wavelength (400 nm) region, indicating lower optical absorption or scattering at a longer wavelength. This feature may arise from better structural homogeneity of the film and a lower concentration of light-scattering domains. On the other hand, the $FSSE_{NaI-65}$ film showed comparatively lower transmittance (%) values than $FSSE_{NaI-27}$, starting from 53% transmittance at 400 nm and achieving 85% at 800 nm. This observation suggests that the $FSSE_{NaI-65}$ film shows an optically dense structure, which is attributed to the higher NaI content leading to enhanced light scattering or absorption as compared to $FSSE_{NaI-27}$. Higher content of NaI in the $FSSE_{NaI-65}$ film may introduce more ionic clusters within the polysaccharide matrix.[23]

Tauc plots were used to estimate the optical band gaps, assuming direct allowed transitions (Fig. 3e and f). The extrapolated linear regions yield optical band gaps of 2.7 eV for $FSSE_{NaI-27}$ and 3.0 eV for $FSSE_{NaI-65}$, respectively. The slight widening of the band gap with the increasing NaI concentration could be attributed to changes in the polysaccharide–salt interactions, which can influence the electronic structure by modifying the polymer chain conformation. The high optical band gaps estimated for the $FSSE_{NaI-27}$ and $FSSE_{NaI-65}$ films indicate negligible electronic conductivity, which is advantageous for the development of purely ion-conducting solid-state electrolytes in device applications. These results demonstrate that both the optical transparency and electronic structure of FSSE films are strongly influenced by the NaI content, offering tuneable properties for applications requiring a combination of ionic conductivity and optical transparency, such as transparent solid-state devices.[39,40]

Electrochemical characterization

Electrochemical impedance spectroscopy (EIS) was conducted at RT to investigate the ionic conductivity of the $FSSE_{NaI-x}$ ($x =$ 27, 43, 53, 60, 65, and 69 wt%) films as a function of the Na^+-ion concentration. The Nyquist plots were fitted using an equivalent circuit model to determine the resistance (R) values (Fig. 4a and S11; Table S4). The obtained 'R' values were then used to determine the ionic conductivity. We estimated the Na^+-ion

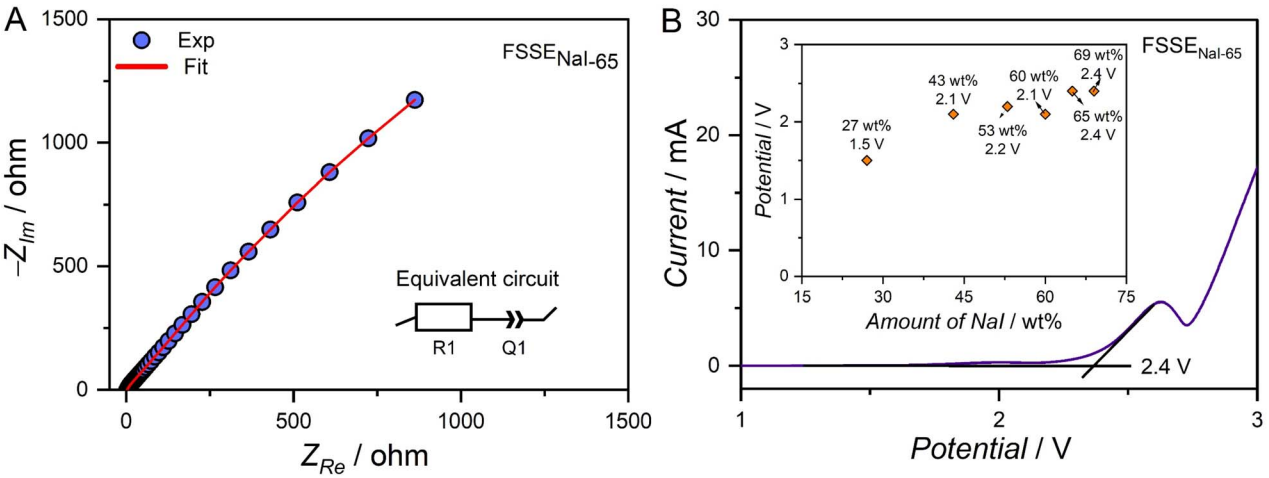

Fig. 4 (a) Nyquist plot of $FSSE_{NaI-65}$. Z_{Re} and Z_{Im} are the real and imaginary components, respectively. The red line indicates the fitting of impedance data by using the specified equivalent circuit. (b) Linear sweep voltammetry (LSV) measurement for $FSSE_{NaI-65}$. (Inset): trends of LSV with the variation of NaI content from 27 wt% to 69 wt%.

conductivity of the synthesized films ($FSSE_{NaI-x}$, $x = 27$, 43, 53, 60, 65, and 69 wt%) which revealed a clear trend of increasing ionic conductivity with the increment in NaI content in the films, reaching a range of superionic conductivity value of 2.77 mS cm^{-1} at 30 °C for $FSSE_{NaI-65}$ (Fig. 4a and Table S4). In addition, $FSSE_{NaI-69}$ showed no further increase in ionic conductivity. This behaviour is attributed to the excessive Na^+-ion concentration which led to the formation of ion aggregates that hindered charge carrier mobility.[41] Additionally, the increased film thickness at higher NaI concentrations may have further contributed to the reduction in effective ion transport.[42] Among all compositions, $FSSE_{NaI-65}$ exhibited the optimal balance between the ion concentration, polymer chain dynamics, and enhanced ion conduction. In contrast, the Na^+-ion conductivity values for other compositions ($FSSE_{NaI-x}$; where $x = 27$, 43, 53, and 60 wt%) were notably lower and they showed limitation in ionic conductivities due to the insufficient amount of mobile Na^+ ions, which constrained the development of continuous ion transport pathways (Table S4). In comparison, other polymer-based electrolytes such as konjac glucomannan with zinc acetate showed an ionic conductivity of 0.56 mS cm^{-1} at room temperature,[43] while poly(vinyl alcohol)/polyacrylonitrile blends with a ceramic filler ($Li_{1.4}Al_{0.4}Ti_{1.6}(PO_4)_3$) exhibited 0.11 mS cm^{-1},[44] and alginate–PVA films achieved around 0.27 mS cm^{-1}.[41] These values highlight the superior ionic conductivity of the $FSSE_{NaI-65}$ film compared to other relevant polymeric systems.

A crucial factor contributing to Na^+-ion conduction in these films is the presence of water molecules, which facilitate the formation of water channels within the polysaccharide network. These hydrated microenvironments play a pivotal role in enabling ion mobility, particularly for Na^+ ions, by supporting transport through hydrogen-bond-assisted pathways.[45,46] To understand the role of water, temperature dependent EIS measurements of the as-synthesized $FSSE_{NaI-65}$ film were conducted under the same electrochemical measurement conditions (Fig. S12–S14). Remarkably, the film exhibited a lowering in the ionic conductivity value from 2.11 to 0.08 mS cm^{-1} with the increase in temperature from 30 to 110 °C (Table S5), respectively, due to removal of water molecules highlighting the essential role of water in maintaining ionic mobility. In contrast, the EIS measurement suggests that the water channels (dynamic hydrogen-bonding network) are fully disrupted in the dehydrated/activated state of $FSSE_{NaI-65}$ (Fig. S15 and Table S6). This observation confirms that the ion conduction mechanism in FSSE is strongly dependent on Na^+ ion–water hydration shell migration through hydrated channels.

To gain deeper insights into the ion dynamics of the electrolyte system, dielectric measurements were performed (Fig. S16). The variation of the real (ε') and imaginary (ε'') parts of permittivity with frequency for different compositions is presented. As the NaI content increases from $FSSE_{NaI-27}$ to $FSSE_{NaI-65}$, ε' decreases gradually, indicating a shift from dominant interfacial polarization toward an enhanced ionic mobility. Within this range, ε'' remains relatively high particularly for $FSSE_{NaI-65}$, which also exhibits the highest ionic conductivity, confirming its superior ion transport capability. For $FSSE_{NaI-69}$, both ε' and ε'' drop noticeably, suggesting that excessive salt induces ion–ion aggregation, thereby reducing ionic mobility and limiting both polarization and conductivity. On the other hand, the AC conductivity (σ_{ac}) increases with frequency for all compositions, displaying a typical dispersion pattern associated with localized ion migration. At low frequencies, σ_{ac} is reduced due to electrode polarization, while at higher frequencies the faster ion movement leads to increased conductivity. Across the entire frequency range, $FSSE_{NaI-65}$ shows the highest conductivity, indicating optimal ion transport. In contrast, $FSSE_{NaI-69}$ exhibits a slight decrease compared to $FSSE_{NaI-65}$; however, $FSSE_{NaI-27}$ shows the lowest conductivity, confirming its limited ionic mobility.[47,48]

The electrochemical stability window (ESW) of the $FSSE_{NaI-x}$ ($x = 27$, 43, 53, 60, 65, and 69 wt%) films was determined using linear sweep voltammetry (LSV). For this measurement, the films were sandwiched between stainless steel (SS) plates, and a potential of 0 to 3 V was applied with a scan rate of 0.1 V s^{-1}. The decomposition point of $FSSE_{NaI-65}$ was indicated by the sharp rise in current around 2.7 V in the LSV curve (Fig. 4b). Consequently, the electrolyte may begin to degrade through processes such as ionic breakdown or interfacial reactions.[41] The variation in the ESW with different NaI concentrations highlights the critical role of Na^+ ions in determining the electrolyte's stability. In $FSSE_{NaI-27}$, the limited number of charge carriers and weak ionic interactions result in poor structural integrity and early decomposition at a low ESW of 1.5 V. As the NaI concentration increases, the availability of Na^+ ions enhances the ionic strength and promotes better ion polymer interactions, contributing to a more stable and robust ionic environment.[28] This stabilizing effect reaches its maxima at 65 wt% NaI, where the ESW extends to 2.4 V indicating improved resistance to electrochemical degradation. Beyond this concentration, however, no further improvement is observed, likely due to excessive Na^+-ion content leading to aggregation or disrupted ion pathways. Therefore, $FSSE_{NaI-65}$ is identified as the optimal composition that provides a favourable balance between high Na^+-ion conductivity and a superior electrochemical stability.

Device fabrication and supercapacitor performance

$FSSE_{NaI-65}$ was used as a solid-state electrolyte to assess its performance for supercapacitor applications through cyclic voltammetry (CV) and galvanostatic charge–discharge (GCD) studies. A symmetric device was assembled using carbon electrodes with $FSSE_{NaI-65}$ placed in between and used for further studies (Fig. 5a1 and a2). The CV curves exhibit a nearly leaf-like shape without any distinct redox peaks, validating the electrical double-layer capacitance (EDLC) with a slight increase in current response and integral area.[16] This indicates that ions accumulate at the electrode surface, forming a double layer. The CV curve gradually increases as the scan rate increases from 20 mV s^{-1} to 100 mV s^{-1}, retaining its shape at higher scan rates that suggests low internal resistance of the electrolyte, enabling efficient charge transfer and ion diffusion (Fig. 5b). Additionally, the minimal distortion in the CV curves implies that the

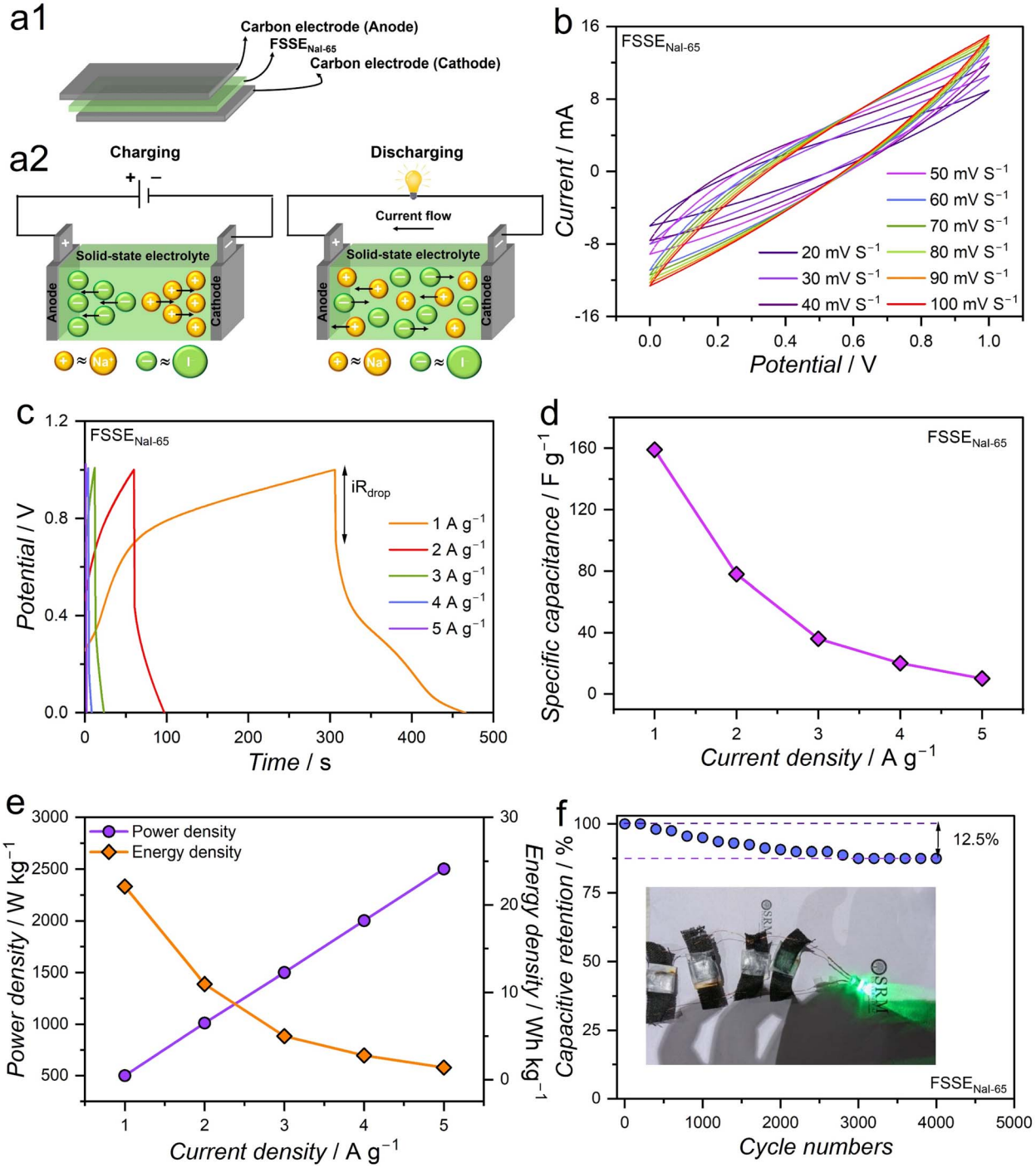

Fig. 5 (a1 and a2) Schematics for a complete cell and charge–discharge mechanism of an EDLC supercapacitor. (b) Cyclic voltammetry curves at various scan rates depicted in the plot. (c) Galvanostatic charge–discharge (GCD) studies at various current densities of 1, 2, 3, 4, and 5 A g^{-1}. (d) Specific capacitance at various current densities. (e) Variation of power and energy densities at different current densities. (f) Cycling stability test at a current density of 5 A g^{-1}. (Inset): digital images of the four parallelly connected devices lighting up one LED.

electrode–electrolyte interface supports rapid ion adsorption and desorption, effectively reducing resistance and diffusion limitations.[16,27]

The GCD studies were carried out at current densities of 1, 2, 3, 4, and 5 A g^{-1}, displaying non-linear behaviour, characteristic of ideal capacitive performance (Fig. 5c and S17).[41] The specific capacitance (C_{sp}) values calculated using eqn (1) (see the Method section in the SI) were 159, 78, 36, 20, and 10 F g^{-1} at the respective current densities (Fig. 5d and Table S7). Furthermore, an increase in iR_{drop} indicates ion transport limitations and resistive losses at the electrolyte/electrode interface, resulting in decreased charge storage efficiency and

a shorter discharge time (Fig. 5c and S17).[41] Besides, the device exhibited energy densities of 22.11, 10.97, 5, 2.78 and 1.39 Wh kg^{-1}, with associated power densities of 501, 1012, 1500, 2001, and 2502 W kg^{-1} at current densities of 1, 2, 3, 4, and 5 A g^{-1} respectively (Fig. 5e). This enhanced electrochemical performance with $FSSE_{NaI\text{-}65}$ is attributed to the interconnected network formed by two polysaccharides (HPMC–KGM), which facilitates efficient ion transport between the electrolyte and electrode surface, thereby improving overall charge storage.

To evaluate the long-term stability of $FSSE_{NaI\text{-}65}$, a cyclability test was conducted up to 4000 cycles (Fig. 5f). The specific capacitance gradually declined with an increase in the number of cycles, retaining 87.5% of its initial value after 4000 cycles (maintaining the same C_{sp} from 3000 cycles onwards), indicating excellent cycle life and durability.

Furthermore, we performed X-ray photoelectron spectroscopy (XPS) analysis to confirm the elemental composition of as-synthesized $FSSE_{NaI\text{-}65}$ (Fig. S19a). The C 1s spectrum shows peaks at 287.6 eV (C=O), 286.2 eV (C–O–C), and 284.7 eV (C–C), whereas the O 1s peaks at 532.8 eV and 531.3 eV correspond to C–O–C and C=O, respectively. Additionally, the I $3d_{3/2}$ (630.1 eV) and I $3d_{5/2}$ (619.3 eV) peaks confirmed the presence of I^-, while Na 1s at 1071.0 eV indicates Na^+.[49] After 4000 charge–discharge cycles, C 1s peaks shift slightly (288.2, 286.2, and 284.0 eV), O 1s remains at 532.9 and 531.4 eV, I 3d shifts to 630.4 and 618.9 eV, and Na 1s shifts to 1071.4 eV, confirming Na^+ stability and the chemical integrity of the $FSSE_{NaI\text{-}65}$ film (Fig. S19b).[50,51] On the other hand, for the pristine carbon electrode, the C 1s peaks appear at 292.4 eV, 287.5 eV (C=O), and 286.5 eV (C–O–C), with O 1s at 533.4 eV (C=O) (Fig. S20a). After 4000 charge–discharge cycles with the NaI-based FSSE, the C 1s and O 1s spectra remain nearly unchanged, confirming excellent interfacial stability and minimal electrolyte decomposition. The C 1s spectrum shows peaks at 292.2, 287.6 (C=O), 286.4 (C–O–C), and 284.8 eV (C–C), while the O 1s spectrum exhibits 534.8 (C–O) and 533.5 eV (C=O). NaI retention in the porous carbon is indicated by I 3d peaks at 632.1 and 620.1 eV and Na 1s peaks at 1071.0 and 1072.8 eV, confirming post-cycling retention of Na^+ species (Fig. S20b).[50,51] The slight performance degradation may be attributed to electrolyte depletion, particularly the formation of a charge depletion layer during the initial cycles. In this phase, some carrier ions can be trapped within the porous structure of the electrode, leading to reduced availability of mobile charge carriers. This results in a depletion region at the electrode–electrolyte interface or on the electrode surface, thereby lowering the effective capacitance. Additional contributing factors could include minor degradation of the electrode material or slow structural changes at the interface over prolonged cycling.[41] Despite these effects, the $FSSE_{NaI\text{-}65}$ based device maintains high capacitance retention and demonstrates strong long-term operational reliability.

Bending electrochemical behaviour of the fabricated supercapacitor

CV curves were recorded at various bending angles, such as 0°, 45°, 90°, 135°, and 180° at a fixed scan rate of 100 mV s^{-1}, to evaluate the electrochemical behaviour under the influence of bending (Fig. 6a and b).

The CV curves are nearly typical leaf-like shape with consistent integral areas and no distinct redox peaks, indicating stable capacitive behaviour under bending. The minimal variation in the CV profiles confirms the mechanical flexibility and reliable

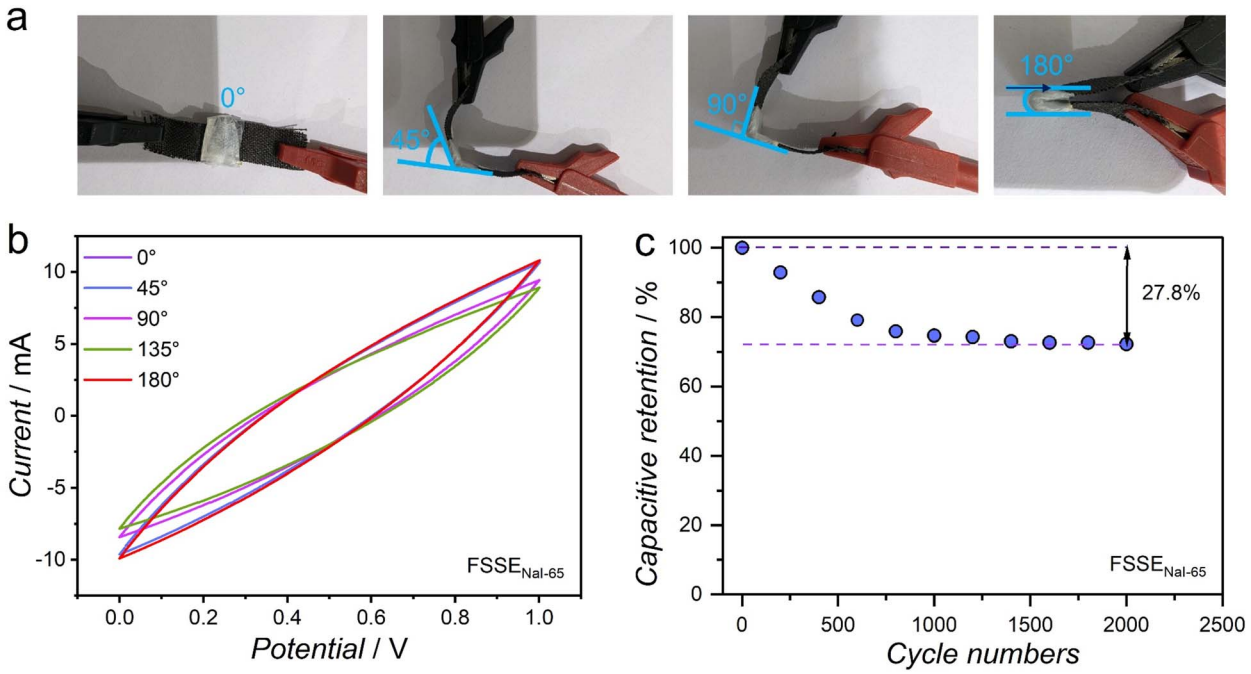

Fig. 6 (a) Digital photographs of an all-solid-state supercapacitor under bending at different angles of 0°, 45°, 90°, and 180°. (b) Cyclic voltammetry curves at 100 mV s^{-1}. (c) Cycling stability test at a current density of 5 A g^{-1} under 90° bending conditions.

electrochemical performance of $FSSE_{NaI-65}$ under stress. GCD was performed at various bending angles (45°, 90°, 135°, and 180°) (Fig. S18 and Table S8). The device maintains efficient specific capacitance along with stable energy and power densities across all bending conditions. The minimal variation in performance demonstrates the excellent mechanical flexibility and interfacial integrity of the $FSSE_{NaI-65}$ electrolyte.

To further evaluate the mechanical durability a bending cycling stability test was performed over 2000 bending cycles at a fixed 90° angle (Fig. 6c). The results showed a negligible loss of 27.8% specific capacitance, confirming the structural integrity and flexibility of $FSSE_{NaI-65}$. Even after repeated bending, the material maintained its charge storage capability, demonstrating its suitability for flexible supercapacitor applications. The ability to sustain high electrochemical performance under continuous mechanical stress highlights the robustness of $FSSE_{NaI-65}$, making it a promising candidate for next-generation flexible and wearable energy storage devices (Fig. S21 and S22 and Tables S9 and S10).

Conclusions

In summary, we developed a series of FSSE films by incorporating varying concentrations of NaI into a dual-biopolymer matrix of KGM and HPMC. Structural analyses using PXRD and FTIR confirmed the formation of homogeneous, amorphous films with effective integration of both polysaccharides. Among the series, the $FSSE_{NaI-65}$ film demonstrated the best mechanical flexibility and electrochemical performance. Optical studies showed that transparency decreased with increasing NaI content, and Tauc plot analysis confirmed wide optical band gaps, indicating negligible electronic conductivity and dominant Na^+-ion transport. Electrochemical impedance spectroscopy revealed superionic conductivity in the range of 10^{-2} to 10^{-4} S cm^{-1} for $FSSE_{NaI-65}$, while linear sweep voltammetry established an electrochemical stability window of 0–2.4 V. Galvanostatic charge–discharge testing showed excellent cycling stability with 87.5% capacitance retention over 4000 cycles, and the device maintained 72.8% of its initial capacitance after 2000 bending cycles, confirming its mechanical robustness and practical applicability. Overall, these findings establish $FSSE_{NaI-65}$ as a promising electrolyte for next-generation flexible, eco-friendly, and solid-state energy storage systems. Future studies may focus on improving device performance by exploring different working electrode materials to enhance interfacial compatibility, designing asymmetric devices to extend the operational voltage window, and assessing the biodegradability and environmental safety of the materials to facilitate their use in sustainable and transient electronics.

Author contributions

C. D. designed the project. S. W. carried out all the material synthesis and characterized the samples by PXRD, FT-IR, and UV-visible spectroscopy. B. J. and M. S. performed the TGA and DSC measurements and C. D. and S. W. analysed the data. S. W., S. S. Y., L. N. P., and P. S. M. carried out all electrochemical characterization and analysed the data. S. G. performed and C. D. analysed the SEM and EDAX spectroscopic data. C. D. and S. W. drafted the initial manuscript. All authors contributed to revising the manuscript. All authors have given approval to the final version of the manuscript.

Conflicts of interest

The authors declare no competing financial interest.

Data availability

The data supporting this article have been included as part of the SI. See DOI: https://doi.org/10.1039/d5ta04374c.

PXRD, FT-IR, Raman, UV-Vis, SEM/EDAX, TGA-DTA, DSC, EIS, and other electrochemical studies have been presented in SI.

Acknowledgements

S. W. appreciates SRM University-AP for receiving a PhD fellowship. C. D. acknowledges the generous funding support from SRM University-AP through the SEED grant (sanction order number: SRMAP/URG/SEED/2023-24/019 and Anusandhan National Research Foundation (ANRF) sponsored PM-ECRG grant (sanction order number: ANRF/ECRG/2024/001345/CS). The authors sincerely thank the Department of Science and Technology (DST), Delhi, India, for providing the NMR facility under the DST-FIST project (SR-FST-CS-I-2021-219(C)).

References

1 A. A. Hor, N. Yadav and S. A. Hashmi, *J. Energy Storage*, 2023, **64**, 107227.
2 H. Heydari and M. B. Gholivand, *New J. Chem.*, 2016, **41**, 237–244.
3 X. Peng, H. Liu, Q. Yin, J. Wu, P. Chen, G. Zhang, G. Liu, C. Wu and Y. Xie, *Nat. Commun.*, 2016, **7**, 11782.
4 S. Konwar, P. K. Singh, P. Dhapola, A. Singh, S. V. Savilov, M. Z. A. Yahya, S. Siyahjani Gultekin and B. Gultekin, *ACS Appl. Electron. Mater.*, 2023, **5**, 5503–5512.
5 S. B. Aziz, P. O. Hama, D. M. Aziz, N. M. Sadiq, H. J. Woo, M. F. Z. Kadir, R. T. Abdulwahid, B. A. Al-Asbahi, A. A. A. Ahmed and J. Hassan, *J. Energy Storage*, 2025, **114**, 115841.
6 J. Zhang, J. Yan, Y. Zhao, Q. Zhou, Y. Ma, Y. Zi, A. Zhou, S. Lin, L. Liao, X. Hu and H. Bai, *Nat. Commun.*, 2023, **14**, 1–12.
7 T. Qin, S. Peng, J. Hao, Y. Wen, Z. Wang, X. Wang, D. He, J. Zhang, J. Hou and G. Cao, *Adv. Energy Mater.*, 2017, **7**, 1–10.
8 K. Li, J. Liu, Y. Huang, F. Bu and Y. Xu, *J. Mater. Chem. A*, 2017, **5**, 5466–5474.
9 A. B. Puthirath, S. Patra, S. Pal, M. Manoj, A. Puthirath Balan, S. Jayalekshmi and N. N. Tharangattu, *J. Mater. Chem. A*, 2017, **5**, 11152–11162.
10 R. Khurana, J. L. Schaefer, L. A. Archer and G. W. Coates, *J. Am. Chem. Soc.*, 2014, **136**, 7395–7402.

11 L. Zhu, J. Chen, Y. Wang, W. Feng, Y. Zhu, S. F. H. Lambregts, Y. Wu, C. Yang, E. R. H. van Eck, L. Peng, A. P. M. Kentgens, W. Tang and Y. Xia, *J. Am. Chem. Soc.*, 2024, **146**, 6591–6603.
12 J. Li, M. Yang, Y. Zhao, W. Zhang, L. Huo, X. Zhang, J. Gao, H. Pang and H. Xue, *ACS Appl. Energy Mater.*, 2021, **4**, 5830–5839.
13 A. Murali, N. Venkatesan, S. Mohan, A. Al Souwaileh, A. S. Roy, M. Raja, R. Kothandaraman, S. J. Park and S. S. Han, *J. Mol. Liq.*, 2025, **426**, 127355.
14 P. Mohapatra and A. K. Barick, *J. Power Sources*, 2025, **626**, 235749.
15 S. Bandyopadhyay, N. Gupta, A. Joshi, A. Gupta, R. K. Srivastava, B. K. Kuila and B. Nandan, *ACS Appl. Energy Mater.*, 2023, **6**, 4390–4403.
16 S. B. Aziz, R. T. Abdulwahid, M. A. Brza, M. B. Ahmed, A. R. Murad, H. B. Tahir, R. M. Abdullah, J. M. Hadi and S. A. Hussen, *J. Energy Storage*, 2023, **71**, 108175.
17 M. Yan, W. Qu, Q. Su, S. Chen, Y. Xing, Y. Huang, N. Chen, Y. Li, L. Li, F. Wu and R. Chen, *ACS Appl. Mater. Interfaces*, 2020, **12**, 13950–13958.
18 S. Chai, Y. Zhang, Y. Wang, Q. He, S. Zhou and A. Pan, *eScience*, 2022, **2**, 494–508.
19 W. Zhao, M. Jiang, W. Wang, S. Liu, W. Huang and Q. Zhao, *Adv. Funct. Mater.*, 2021, **31**, 1–30.
20 S. W. Kim and S. Y. Lee, *Energy Environ. Mater.*, 2020, **3**, 265–285.
21 J. Seo, G. Han, H. Kim and D. Lee, *Sci. Rep.*, 2022, **12**, 1–7.
22 A. Takemoto, T. Araki, K. Nishimura, M. Akiyama, T. Uemura, K. Kiriyama, J. M. Koot, Y. Kasai, N. Kurihira, S. Osaki, S.-i. Wakida, J. M. J. den Toonder and T. Sekitani, *Adv. Sci.*, 2023, **10**, 1–11.
23 J. Zhi, M. Zhou, Z. Zhang, O. Reiser and F. Huang, *Nat. Commun.*, 2021, **12**, 1–12.
24 Y. Guo, W. Guan, C. Lei, H. Lu, W. Shi and G. Yu, *Nat. Commun.*, 2022, **13**, 1–7.
25 K. Jayalakshmi, S. Hegde and J. Monteiro, *J. Energy Storage*, 2024, **89**, 111575.
26 H. Zheng, H. Zhou, C. Wei, B. Zheng, Y. Gao, Z. Wang, H. Zhang, A. Ma, X. Jin and H. Liu, *ACS Appl. Eng. Mater.*, 2023, **1**, 1375–1383.
27 R. T. Abdulwahid, S. B. Aziz and M. F. Z. Kadir, *Mater. Today Sustain.*, 2023, **23**, 100472.
28 S. K. Shetty, Ismayil, P. Nayak, Y. N. Sudhakar and I. M. Noor, *J. Energy Storage*, 2024, **95**, 112553.
29 H. Chen, L. Zhou, Y. Sun, T. Zhang, H. Wang, H. Huang, J. Ning and Y. Hu, *Energy Storage Mater.*, 2025, **76**, 104113.
30 C. Tian, J. Wang, R. Sun, T. Ali, H. Wang, B.-B. Xie, Y. Zhong and Y. Hu, *Angew. Chem., Int. Ed.*, 2023, **62**, e202310970.
31 S. Huang, L. Hou, T. Li, Y. Jiao and P. Wu, *Adv. Mater.*, 2022, **34**, 2110140.
32 K. I. Hadjiivanov, D. A. Panayotov, M. Y. Mihaylov, E. Z. Ivanova, K. K. Chakarova, S. M. Andonova and N. L. Drenchev, *Chem. Rev.*, 2021, **121**, 1286–1424.
33 Y. Chen, Y. Wang, Z. Li, D. Wang, H. Yuan, H. Zhang and Y. Tan, *Compos. Commun.*, 2021, **26**, 100774.
34 S. Ding, C. Fang, X. Wang and Z. Wang, *Polymer*, 2020, **186**, 121993.
35 R. Rahmawati, S. Nozaki, K. Kojio, A. Takahara, N. Shinohara and S. Yamasaki, *Polym. J.*, 2019, **51**, 265–273.
36 X.-W. Huang, S.-Y. Liao, Y.-D. Liu, Q.-S. Rao, X.-K. Peng and Y.-G. Min, *Electrochim. Acta*, 2021, **389**, 138747.
37 H. Wang, C. Lin, X. Yan, A. Wu, S. Shen, G. Wei and J. Zhang, *J. Electroanal. Chem.*, 2020, **869**, 114156.
38 F. Zeng, Y. Sun, B. Hui, Y. Xia, Y. Zou, X. Zhang and D. Yang, *ACS Appl. Mater. Interfaces*, 2020, **12**, 43805–43812.
39 D. M. Mamand, D. S. Muhammad, D. Q. Muheddin, K. A. Abdalkarim, D. A. Tahir, H. A. Muhammad, S. B. Aziz, S. A. Hussen and J. Hassan, *Sci. Rep.*, 2025, **15**, 3162.
40 N. M. Farrage, N. H. Teleb and W. A. Abd El-Ghany, *Opt. Quantum Electron.*, 2024, **56**, 1–20.
41 N. M. Ghazali, N. F. Mazuki, M. H. Sulaiman, K. Aoki, Y. Nagao and A. S. Samsudin, *Solid State Ionics*, 2024, **414**, 116650.
42 B. X. Dong, P. Bennington, Y. Kambe, D. Sharon, M. Dolejsi, J. Strzalka, V. F. Burnett, P. F. Nealey and S. N. Patel, *Mol. Syst. Des. Eng.*, 2019, **4**, 597–608.
43 N. Chiaoprakobkij, M. Okhawilai, P. Kasemsiri and H. Uyama, *Int. J. Biol. Macromol.*, 2024, **273**, 133204.
44 H. K. Tran, Y. S. Wu, W. C. Chien, S. H. Wu, R. Jose, S. J. Lue and C. C. Yang, *ACS Appl. Energy Mater.*, 2020, **3**, 11024–11035.
45 R. Sujanani, P. H. Nguyen, L. W. Gordon, J. T. Bamford, A. Zele, B. J. Pedretti, N. A. Lynd, R. J. Clément and R. A. Segalman, *ACS Macro Lett.*, 2025, **14**, 64–71.
46 T. Yan, Y. Zou, X. Zhang, D. Li, X. Guo and D. Yang, *ACS Appl. Mater. Interfaces*, 2021, **13**, 9856–9864.
47 C. Maheshwaran, D. K. Kanchan, K. Mishra, D. Kumar and K. Gohel, *Nano-Struct. Nano-Objects*, 2020, **24**, 100587.
48 A. C. Radjendirane, D. K. Maurya, S. P. Rajendra, M. S. AlSalhi, Z. Guo and S. Angaiah, *J. Phys. Chem. C*, 2024, **128**, 6950–6961.
49 D. Shrestha, S. Maensiri, U. Wongpratat, S. W. Lee and A. R. Nyachhyon, *J. Environ. Chem. Eng.*, 2019, **7**, 103227.
50 K. Chen, H. Huang, S. Xu, Z. Yuan, Y. Yang, Y. Yao, X. Zhang, X. Rui and Y. Yu, *Carbon Neutrality*, 2024, **3**, 7.
51 F. Wang, Z. Jiang, Y. Zhang, Y. Zhang, J. Li, H. Wang, Y. Jiang, G. Xing, H. Liu and Y. Tang, *eScience*, 2024, **4**, 100181.